WIND ENERGY
Wind Energ. 2008; **11**:245–264
Published online 7 January 2008 in Wiley Interscience
(www.interscience.wiley.com) DOI: 10.1002/we.262

HAWT Near-Wake Aerodynamics, Part I: Axial Flow Conditions

Wouter Haans*, Faculty of Aerospace Engineering, Delft University of Technology, Kluyverweg 1, 2629 HS, Delft, The Netherlands
Tonio Sant, Faculty of Aerospace Engineering, Delft University of Technology, Kluyverweg 1, 2629 HS, Delft, The Netherlands and Faculty of Engineering, University of Malta, Tal-Qroqq, MDS 07, Msida, Malta
Gijs van Kuik and Gerard van Bussel, Faculty of Aerospace Engineering, Delft University of Technology, Kluyverweg 1, 2629 HS, Delft, The Netherlands

Key words:
rotor aerodynamics; rotor experiments; yaw; near-wake; hot-wire anemometry

An improved physical understanding of the rotor aerodynamics of a horizontal axis wind turbine (HAWT) is required to reduce the uncertainties associated with today's design codes. Wind tunnel experiments contribute to increased knowledge and enable validation and construction of models. The present study focuses on the near-wake of a model HAWT in both axial and yawed flow conditions. At three downstream planes parallel to the rotor plane, single-sensor hot-film traverses are made. The phase-locked unsteady three-dimensional flow velocity vector is determined by a novel data reduction method. A series of two papers discusses the near-wake aerodynamics of a model HAWT. The main goals are to obtain a detailed understanding of the near-wake development and to arrive at a base for model construction and validation. The first paper presents the experimental setup, data reduction and the results for the baseline case (axial flow conditions). In the second paper, the results for the yawed flow cases are presented and the effect of yaw misalignment on the near-wake development is discussed. Copyright © 2008 John Wiley & Sons, Ltd.

Received 10 July 2006; Revised 17 October 2007; Accepted 26 October 2007

Introduction

The rotor aerodynamics of a horizontal axis wind turbine (HAWT) consists of strongly coupled blade and wake aerodynamics. Hence, for accurate predictions of HAWT performance and loads, adequate modelling of the wake and blade aerodynamics is essential. To reduce the uncertainties of today's design codes, the need for an improved physical understanding of rotor aerodynamics is generally acknowledged.[1–3] Advanced rotor aerodynamics codes, such as vortex wake codes and Reynolds-averaged Navier–Stokes codes, and experiments in controlled conditions, hence in wind tunnels, contribute to increased knowledge. Furthermore, wind tunnel measurements are required to validate rotor aerodynamics codes and could be used to construct models as well.

Combined blade load and rotor wake recordings are desired because of the coupling between the blade and wake aerodynamics. In general, however, measurements focus either on the rotor wake or on the blade loads. In the present study, rotor wake measurements are discussed. The experiments, conducted at the Delft University of Technology (TUDelft), focus on the near-wake behind a model HAWT subject to both axial and yawed flow conditions.

* Correspondence to: W. Haans, Faculty of Aerospace Engineering, Delft University of Technology, Kluyverweg 1, 2629 HS, Delft, The Netherlands.
E-mail: w.haans@lr.tudelft.nl

Axial flow conditions form the baseline for yawed flow conditions. Whereas axial flow conditions yield nearly axisymmetric flow with the rotor operating in the wind turbine state, yawed flow conditions are characterized by cyclic flow unsteadiness and a non-axisymmetric wake. Yaw misalignment is relevant as it occurs frequently on full-scale HAWTs, poses a challenge for today's rotor aerodynamics codes[4] and can be tested in a wind tunnel.

A limited number of wind tunnel experiments focused on the wake of model HAWTs have been performed. For a recent overview of rotor aerodynamics studies in axial flow conditions, see Vermeer *et al.*[5] An extensive experimental study of the near-wake three-dimensional velocity field downstream of a model rotor in axial flow conditions was performed by Ebert and Wood[6–8] using phase-locked average (PLA, also referred to as ensemble average) hot-wire constant-temperature anemometry (CTA). However, large, uncorrected wind tunnel wall effects complicate comparison with models; the turbine diameter equals the 'diameter' of the octagonal open jet outlet. The measurement domain is given by $z/R_t = (0.08; 0.80)$, with z the axial distance from the rotor plane and R_t the radius of the rotor blade tip. These measurements were used to compare velocity trends found in the current experiments.

Regarding yawed flow conditions, the tip vortices in the wake of model rotors are both visualized[9] and measured with particle image velocimetry (PIV)[10] to study the skewed tip vortex geometry. PIV is also used to determine the velocity and circulation of the tip vortices[11] and to measure the downstream development of time-averaged axial velocity profiles in the wake.[12]

Evidence of low-frequency wake meandering, similar to bluff body vortex shedding, was found by Medici and Alfredsson[13] for both axial and yawed flow conditions using hot-wire CTA in the far wake, with $z/R_t \geq 2$. The downstream extent of current measurements is $z/R_t \leq 0.15$. Because of the proximity to the rotor plane, the flow is considered cyclic with the rotor blade frequency and the effect of possible low-frequency wake meandering is neglected.

Vermeer performed wake studies on the same model rotor and open jet wind tunnel used for the current experimental campaign, see Reference 14 for an overview of Vermeer's work.[14] PLA hot-wire CTA in the near-wake is used to derive an engineering inflow model for yawed conditions.[15] Hot-film measurements in the present study are more extensive, utilize a novel data reduction method and are analysed in more detail than Vermeer's experiments. However, Vermeer's experimental database provides an excellent opportunity to check repeatability.

The present hot-film measurements are part of a larger experimental campaign, using a multitude of measurement techniques; for a range of operating conditions, with both zero and non-zero yaw angles, the thrust coefficient is determined from strain gauge recordings, and a general overview of the wake geometry is obtained by quantitative smoke visualization of the tip vortices.[16] A limited subset from the range of operating conditions is selected for study in more detail. Tuft visualizations on the blade are performed, in conjunction with hot-film CTA in the near-wake, to observe dynamically stalled flows.[17] Furthermore, the PLA three-dimensional flow velocity vectors in the near-wake are determined by means of hot-film CTA. At three downstream planes parallel to the rotor plane, single-sensor hot-film traverses are made. A novel data reduction method enables the derivation of the PLA three-dimensional flow velocity vector, as discussed in Haans *et al.*,[18] where a brief overview of results is given as well.

This series of two papers concerns the hot-film CTA measurements. The two main research goals are obtaining a detailed understanding of the flow development in the near-wake and arriving at a base for model construction and validation. Consequently, the flow conditions are well documented and the data reduction includes corrections for wind tunnel wall effects and estimates of the measurement uncertainty. After presenting the experimental setup and the data reduction, this first paper discusses the near-wake aerodynamics of the baseline axial flow case. The second paper will treat the effect of yaw misalignment.

Experiments

Setup and Conditions

Hot-film measurements in the near-wake of a rotor model are performed in an open jet wind tunnel at the TUDelft. A schematic of the setup, including the global cartesian and cylindrical coordinate systems, attached

DOI: 10.1002/we

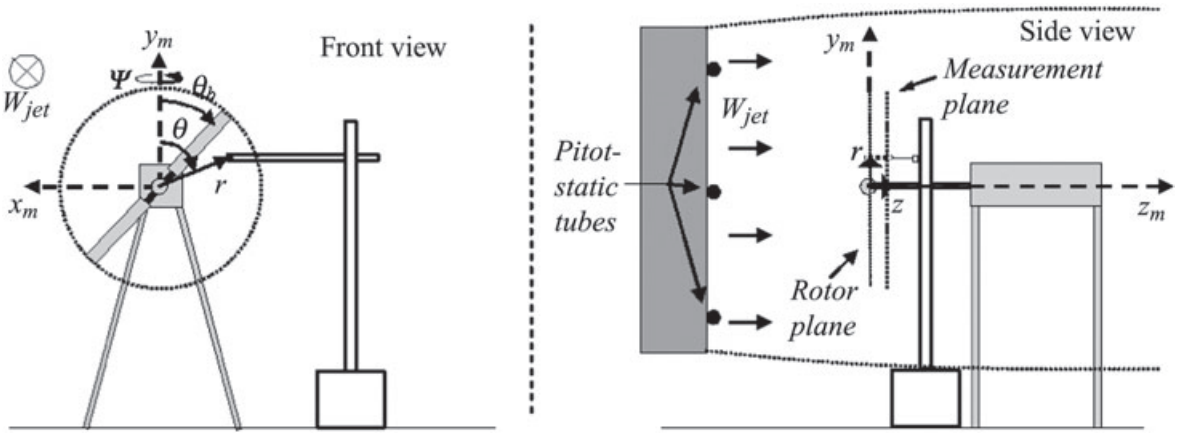

Figure 1. Schematic of the experimental setup. The rotor model, traversing rig and wind tunnel exit with the Pitot-static tubes are shown. Both the global cartesian coordinate system (x_m, y_m, z_m) and the global cylindrical coordinate system (r, θ, z) are attached to the non-rotating model support. θ_b is the blade azimuth angle, Ψ is the yaw angle, and y_m is the yaw axis

Table I. Rotor main geometric features

Number of blades	2	
Airfoil section	NACA0012	
Rotor radius R_t (m)	0.6	
Blade root radius R_r (m)	0.18	
Chord c (m)	0.08 (constant)	
Blade pitch angle θ_c (°)	$\theta_c(r/R) = (6 + \theta_{c_{tip}}) - 6.67 \cdot r/R$	$0.3 \le r/R \le 0.9$
	$\theta_c(r/R) = \theta_{c_{tip}}$	$0.9 < r/R \le 1$

to the non-rotating model support, is shown in Figure 1. Readings from three interconnected Pitot-static tubes mounted in the jet exit plane, combined with ambient pressure and jet temperature recordings, yield the velocity magnitude in the jet exit plane $|\vec{V}_{jet-exit}|$, when applying the perfect gas law and Bernoulli's equation. The flow is assumed to have an axial component only, $|\vec{V}_{jet-exit}| = W_{jet}$.

The main characteristics of the open jet wind tunnel are a diameter of the jet exit plane of 2.24 m, a maximum attainable wind speed $W_{jet,max}$ of 14.5 m s^{-1} and a freestream turbulence intensity Tu of 1.2 ± 0.2% at $W_{jet} = 5.5$ m s^{-1}, the speed at which the measurements are taken. The wind tunnel is not equipped with a separate return channel; the hall is used for recirculation instead.

The main geometric features of the two-bladed rotor model are given in Table I. The model offers the possibility of altering the blade pitch angle automatically, by modifying the tip pitch angle $\theta_{c_{tip}}$. The axial force T on the rotor, the force normal to the rotor plane, is recorded by means of strain gauges on the rotor shaft. The rotor plane is positioned 1 m downstream of the jet exit plane, with the rotor hub in line with the jet centre. The distance from the rotor plane to the downstream tunnel wall is 11 m or 18.4 rotor radii R_t.

The unsteady velocity field in the near-wake of the rotor model is measured using hot-film CTA. A single-film hot-film probe is mounted on a traversing rig that makes an automated traverse through a plane parallel to the rotor plane. Two similar types of single-film hot-film probes are used, apart from the hot-film orientation: the 'normal' type, with the hot-film perpendicular to the probe (TSI 1201-20), and the 'parallel' type with the hot-film parallel to the probe (TSI 1211-20)—see Figure 2. The probes are manufactured by TSI Incorporated, located in Shoreview, MN.

The main characteristics of the hot-film probes are given in Table II. The hot-film recordings are synchronized with the rotational frequency of the blades. The measurement resolution of $\Delta\theta_b = 2$ corresponds to

DOI: 10.1002/we

Figure 2. The normal and parallel types of single-film hot-film probes. For each type, the local cartesian coordinate system (x_p, y_p, z_p), attached to the probe, is included

Table II. Hot film main characteristics

Hot-film material	Platinum film on fused-quartz substrate
Hot-film diameter (μm)	50.8
Hot-film length (mm)	1.02
Upper frequency limit (kHz)	75 @ 10 m s^{-1} [19]
Probe diameter (mm)	3.9

approximately 2.1 kHz. Hence, the frequency resolution is 1.0 kHz. The CTA upper frequency limit depends on the flow velocity; at 10 m s^{-1}, which is at the same order of magnitude as the flow velocity experienced in the near-wake experiments, a value of approximately 75 kHz is found for CTA using a cylindrical hot-film.[19] The frequency resolution is hence significantly smaller than the upper frequency limit.

The yaw angle Ψ, being the angle between the normal vector to the rotor plane and the undisturbed velocity vector, is set to 0° in order to obtain the axial flow condition studied in this paper. The blades rotate at $f = 11.67$ Hz and W_{jet} is set to 5.5 m s^{-1}. Hence, the tip speed ratio λ, defined as

$$\lambda = \frac{2\pi f R_t}{W_{jet}} \tag{1}$$

is 8. θ_{ctip} is fixed at 2°. The power coefficient c_P and thrust coefficient c_T of the rotor model are given by

$$c_P = \frac{P}{\frac{1}{2}\rho W_{jet}^3 \pi R^2} \tag{2}$$

and

$$c_T = \frac{T}{\frac{1}{2}\rho W_{jet}^2 \pi R^2} \tag{3}$$

respectively, with P representing the rotor power and ρ the air density. A performance study by Vermeer[14] with the rotor model set to a range of values for λ and $\theta_{c_{tip}}$ shows that the currently selected operating condition of $\Psi = 0°$, $\lambda = 8$, $\theta_{c_{tip}} = 2°$ yields $c_{P_{max}}$, with $c_{P_{max}} = 0.32$. Measurements by Haans *et al.*[16] yield $c_T = 0.80$ at the currently selected operating condition.

For a point fixed on the blade, located at $0.7R_t$, the chord Reynolds number $Re_{0.7R}$ is determined. To estimate $Re_{0.7R}$, the flow velocity relative to the blade is assumed to consist of the undisturbed velocity and the blade rotation components only. $Re_{0.7R}$ is written as

$$Re_{0.7R} = \frac{c\sqrt{W_{jet}^2 + (2\pi f 0.7R_t)^2}}{\nu} \tag{4}$$

with c the airfoil chord and ν the kinematic viscosity. $Re_{0.7R} = 1.6 \times 10^5$ is found. As argued by Vermeer *et al.*,[5] the low Re compared with that of a full-scale wind turbine is acceptable since the characteristics of the

DOI: 10.1002/we

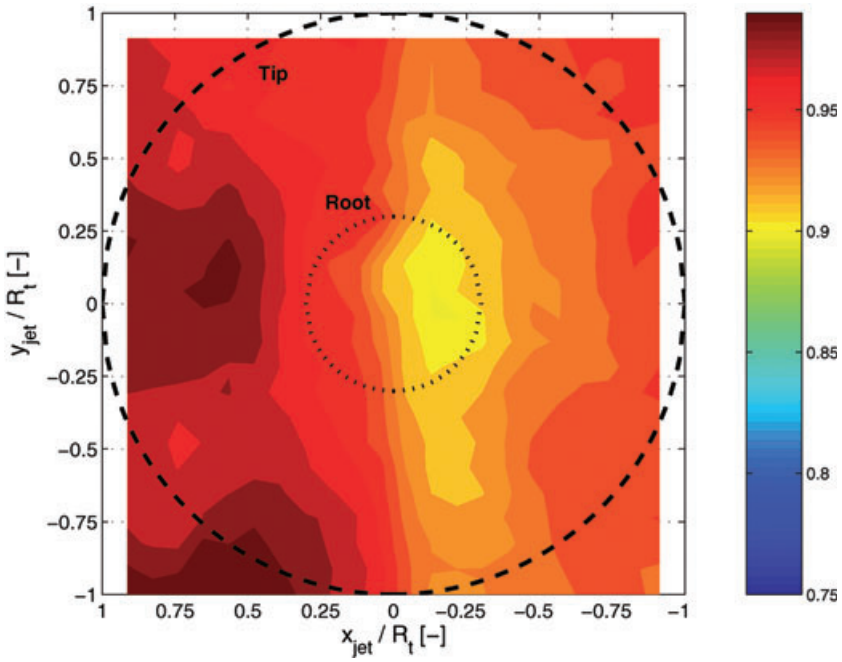

Figure 3. $W/W_{je-exit}$ *measured in the empty tunnel, at the rotor plane location, normalized with the maximum value of* W/W_{jet}. *The jet is set to* $W_{jet} = 5.5\ m\ s^{-1}$. *Included are the outlines of the model rotor tip and root. Viewpoint is from upwind*

NACA0012 airfoil are known for the *Re*-range on the model rotor. The experimental results can still be used for comparison with and validation of numerical models.

Note that the turbulence intensity for a point fixed on a rotating blade is reduced compared with the freestream turbulence intensity as a consequence of the increased apparent flow velocity due to blade rotation. The blade rotates through a non-uniform, non-axisymmetric freestream flow field (however, see Figure 3), resulting in additional 'turbulence' at a point fixed on the blade. The axial velocity reduction near the centre of the jet is associated with the wake trailed from the nacelle of the wind tunnel fan that is located upstream of the test section.

Procedure

Estimates of the velocity magnitude and direction require hot-film measurements at multiple orientations.[19] The current research concerns the PLA flow velocity, $\langle \vec{V} \rangle$ (r, θ, z, θ_b), instead of quantitative turbulence data or the instantaneous flow velocity V. A single-film hot-film probe requires successive measurements at varying probe orientations to estimate $\langle \vec{V} \rangle$. A three-film type hot-film probe can yield the instantaneous $\langle \vec{V} \rangle$. Both measurements with the single- and three-film type hot-film require the flow conditions to be constant throughout the experimental campaign. An additional requirement for the single-film type hot-film is the repeatability of the (r, θ, z)-coordinate and of the θ_b-phase, as multiple recordings at a given (r, θ, z, θ_b)-point are needed to estimate $\langle \vec{V} \rangle$ (r, θ, z, θ_b). Because of its relative inexpensiveness, expendability and ease of calibration, the single-film type probe is preferred to the three-film type probe.

Hot-film measurements are performed in one plane 6.0 cm upstream of the rotor plane and three downstream planes, at 3.5 cm $(0.0583R_t)$, 6.0 cm $(0.10R_t)$ and 9.0 cm $(0.15R_t)$ from the rotor plane. The spatial resolution of the measurement points, in cylindrical coordinates, is given by r = 0.24, 0.30, 0.36, . . . 0.60 m (r/R_t =

DOI: 10.1002/we

0.4, 0.5, 0.6, . . . 1), $\theta = 0^\circ$, 15°, 30° . . . 345°. For a given (r, θ, z)-location, a hot-film reading is taken with a resolution of $\Delta\theta_b = 2^\circ$, for a total of 54 rotational cycles, resulting in 54 recordings per (r, θ, z, θ_b)-point. Concurrent with the hot-film recordings, W_{jet} and f are logged every cycle, yielding a total of 54 recordings per (r, θ, z)-location.

A sample size of 54 hot-film recordings is adequate; the uncertainty associated with the determination of the PLA yields a minor contribution to the total experimental uncertainty of $\langle\vec{V}\rangle$, as is discussed later. Previous hot-film experiments in the wake of the same rotor model[14] indicate that a measurement resolution of $\Delta\theta_b = 2^\circ$ is sufficient to capture the PLA velocity variations observed with both blade and wake passages.

At a given (r, θ, z, θ_b)-location, six CTA measurements each with a different orientation of the hot-film, are required for the data reduction technique proposed in Haans *et al.*[18] to determine the PLA flow velocity. Because of the limited range of the traversing rig, a 30 minutes measurement run covers half of the measurement plane. Errors between intended and true (r, θ, z)-positions due to random shifts of the traversing rig accumulate and result into an offset when returning to the starting point upon completion of a traverse. After each traverse, the offset is determined and the hot-film probe is reset to the correct starting point.

The sensitivity of the hot-film output voltage E to the speed and direction of the fluid flow is determined with speed and angular calibrations, respectively. For speed calibrations, the hot-film is positioned normal to the direction of the flow. Angular calibrations determine the relation between E and flow angle for a given speed. Both speed and angular calibrations are performed regularly to compensate for hot-film ageing.

Data Reduction

Before discussing the data reduction in detail, it must be noted that three coordinate systems are utilized; the hot-film probe fixed cartesian coordinate system (x_p, y_p, z_p)—see Figure 2—and the two rotor support fixed coordinate systems, a cartesian one (x_m, y_m, z_m) and a cylindrical one (r, θ, z)—see Figure 1.

Velocity Determination

Speed and angular calibrations of the hot-film anemometers form the basis for velocity determination. The temperature-corrected King's Law[19] is used during speed calibration to relate E with W_p, the flow velocity in the z_p direction,

$$E^2 = (T_f - T_a)\left(A + BW_p^n\right) \tag{5}$$

with T_f and T_a the preset hot-film and measured flow temperature, respectively. A, B and n are calibration constants. Generally, the flow velocity is unknown beforehand. The recorded E is thus related to the velocity magnitude when the flow would have been normal to the film, named effective velocity V_{eff}, using equation (5) with $V_{eff} = W_p$. The basis for angular calibration forms Jørgensen's equation,[19]

$$V_{eff}^2 = h^2U_p^2 + k^2V_p^2 + W_p^2 \tag{6}$$

h and k are angular calibration constants that are determined during the angular calibration.

For a comprehensive overview of calibration procedures, see Bruun's work.[19] The techniques applied for the current measurement campaign are presented in Haans *et al.*[18] As the employed calibration procedures are standard practice, they are not discussed in detail here.

Traditional Single-sensor Hot-film Data Reduction Method

The derivation of $\langle\vec{V}\rangle$ with single-film hot-film type probes traditionally uses successive measurements with three orientations of the hot-film probe. Two measurements are taken with the normal probe, one with the parallel probe. For both normal probe orientations, the hot-film is normal to the axial direction (z_p parallel to z_m). For one of the two normal probe orientations, the hot-film is positioned vertically (y_p parallel to y_m, x_p parallel to x_m). For the other normal probe orientation, the hot-film is positioned horizontally (x_p parallel to y_m;

DOI: 10.1002/we

y_p parallel to x_m). The hot-film of the parallel probe is oriented axially (y_p parallel to z_m); the plane formed by the prongs and hot-film is vertical (x_p parallel to x_m, z_p parallel to y_m).

For each(r, θ, z, θ_b)-point and each hot-film orientation, the PLA of equation (6) is taken, where contributions from the disturbance terms, $\langle v_i^2 \rangle$, are neglected as $\langle v_i^2 \rangle$ is, generally, several orders of magnitude smaller than $\langle V_i \rangle^2$

$$\langle V_{eff} \rangle^2 = h^2 \langle U_p \rangle^2 + k^2 \langle V_p \rangle^2 + \langle W_p \rangle^2 \tag{7}$$

A system of equations can be constructed for the three orientations per(r, θ, z, θ_b)-point,

$$\begin{bmatrix} h_1^2 & k_1^2 & 1 \\ k_2^2 & h_2^2 & 1 \\ h_3^2 & 1 & k_3^2 \end{bmatrix} \begin{bmatrix} \langle U_m \rangle^2 \\ \langle V_m \rangle^2 \\ \langle W_m \rangle^2 \end{bmatrix} = \begin{bmatrix} \langle V_{eff,1} \rangle^2 \\ \langle V_{eff,2} \rangle^2 \\ \langle V_{eff,3} \rangle^2 \end{bmatrix} \tag{8}$$

and solved for $\langle U_m \rangle^2$, $\langle V_m \rangle^2$ and $\langle W_m \rangle^2$. Since squared velocity components are determined, the direction of the velocity vector is not part of the solution and has to be estimated. For axial flow conditions, the axial velocity component is large throughout the wake and it can readily be assumed that $\langle W_m \rangle > 0$. However, the velocity components in the rotor plane, $\langle U_m \rangle$ and $\langle V_m \rangle$, are generally small compared with the axial velocity component, and their directions are unknown beforehand. Furthermore, the combined effect of small $\langle U_m \rangle$ and $\langle V_m \rangle$ values and measurement uncertainties yield $\langle U_m \rangle^2 < 0$ and/or $\langle V_m \rangle^2 < 0$ at several (r, θ, z, θ_b)-points. This is clearly a non-physical result.

New Single-sensor Hot-film Data Reduction Method

The two problems of the traditional velocity determination method, the inability to predict the direction of the $\langle U_m \rangle$ and $\langle V_m \rangle$ components and non-physical $\langle U_m \rangle^2$ and $\langle V_m \rangle^2$ values, are overcome by a new method to determine the PLA flow velocity from single-film hot-films. Only the basics are presented here; for a more detailed discussion on the new method, see Haans *et al.*[18] First, it must be noted that the determination of both the magnitude and the direction of $\langle W_m \rangle$ is identical to the approach of the traditional method; the magnitude is estimated using equation (8), the direction of $\langle W_m \rangle$ is assumed to be $\langle W_m \rangle > 0$.

Asymmetry in the response of the parallel hot-film probe to the flow angle in the (y_p, z_p)-plane is observed during angular calibrations (see Figure 4). The determination of both the direction and the magnitude of the $\langle U_m \rangle$ and $\langle V_m \rangle$ components in the new method is based upon the observed asymmetry.

For a given (r, θ, z, θ_b)-point, a total of four probe orientations are used for the parallel probe measurements. The two probe orientations in the (y_m, z_m)-plane are given in Figure 5, and two similar orientations are used in the (x_m, z_m)-plane. The sign of the $\langle V_m \rangle$-velocity component is estimated by comparison of the $\langle V_{eff} \rangle$-signals from the two orientations shown in Figure 5; the smallest value corresponds to the probe orientation where the sensor is shielded from the $\langle V_m \rangle$-component of the flow velocity by its prongs. Similar reasoning holds for $\langle U_m \rangle$, with the two probe orientations in the (x_m, z_m)-plane.

The magnitudes of $\langle U_m \rangle$ and $\langle V_m \rangle$ are determined sequentially. The equation solved for each velocity component is based upon two elements: the unshielded (default) situation modelled with equation (7) and the ratio of $\langle V_{eff} \rangle$ measurements with the probe shielded and unshielded.

Uncertainty

The quality of the experimental results is assessed with an analysis of the measurement uncertainty, using the methodology suggested by the American Institute of Aeronautics and Astronautics (AIAA). After a brief introduction into the terminology used, the results of the analyses of the measurement uncertainty of c_T and $\langle \vec{V} \rangle$ are presented here. For an in-depth discussion of the methodology, see the AIAA measurement uncertainty standard[20] and guide.[21]

The experimental error ε is defined as the difference between the experimentally determined value and the true value of a quantity. The true value is generally unknown; hence, ε must be estimated by an uncertainty U,

DOI: 10.1002/we

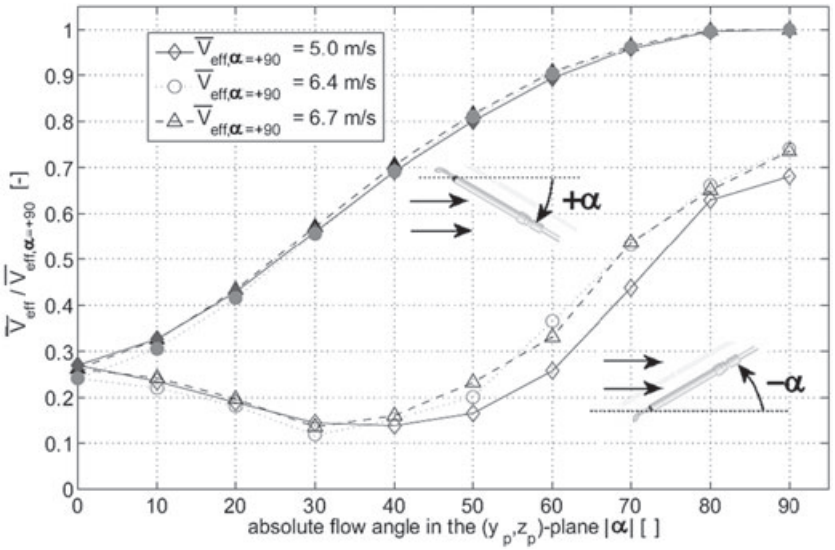

Figure 4. Measurements with the parallel probe: The absolute flow angle α versus the ratio of mean effective velocity $\overline{V}_{eff}$ to mean effective velocity for the $\alpha = +90^\circ$ orientation $\overline{V}_{eff,\alpha=+90^\circ}$. The asymmetry of the probe response to a given flow angle can clearly be observed

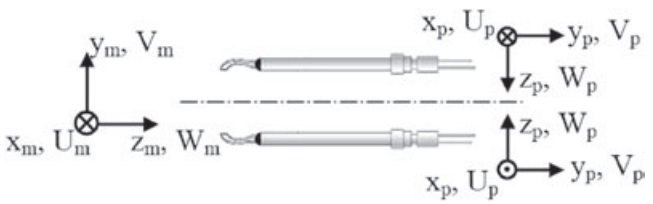

Figure 5. The two parallel probe orientations in the (y_m, z_m)-plane, used for determining the direction of the V_m-component

at a confidence level specified by the experimenter; the default 95% confidence interval is used for the current analyses. U is the orthogonal summation of the systematic uncertainty B and random uncertainty P,

$$U = \left(B^2 + P^2\right)^{1/2}. \tag{9}$$

An uncertainty is classified as random when it contributes to the data scatter with repeated measurements; else, it is a systematic uncertainty.

The systematic and random uncertainty of c_T, B_{c_T} and P_{c_T} respectively, are estimated at $B_{c_T} = 0.078$ and $P_{c_T} = 0.021$, which results in a measurement uncertainty of c_T of $U_{c_T} = 0.081$. With $c_T = 0.80$, U_{c_T} hence is estimated at 10%.

The three-dimensional PLA flow velocity $\langle\vec{V}\rangle$, derived through the new data reduction method, is expressed in the cartesian non-rotating model coordinate system (x_m, y_m, z_m)—see Figure 1 for the experimental setup. $\langle\vec{V}\rangle$ is subsequently made dimensionless by division through W_{jet}. The experimental uncertainty $U_{\langle V\rangle}$ is estimated at the 95% confidence level for each of the three components of the dimensionless PLA flow velocity, at each measured (r, θ, z, θ_b)-point.

The typical range of the measurement uncertainty is $0.09 \lesssim U_{\langle V\rangle} \lesssim 0.17$. The constituting systematic and random uncertainties are estimated at $0.04 \lesssim B_{\langle V\rangle} \lesssim 0.15$ and $P_{\langle V\rangle} = 0.08$, respectively. $P_{\langle V\rangle}$ is thus assumed to be constant, independent of the velocity component and the (r, θ, z, θ_b)-point under consideration. The

DOI: 10.1002/we

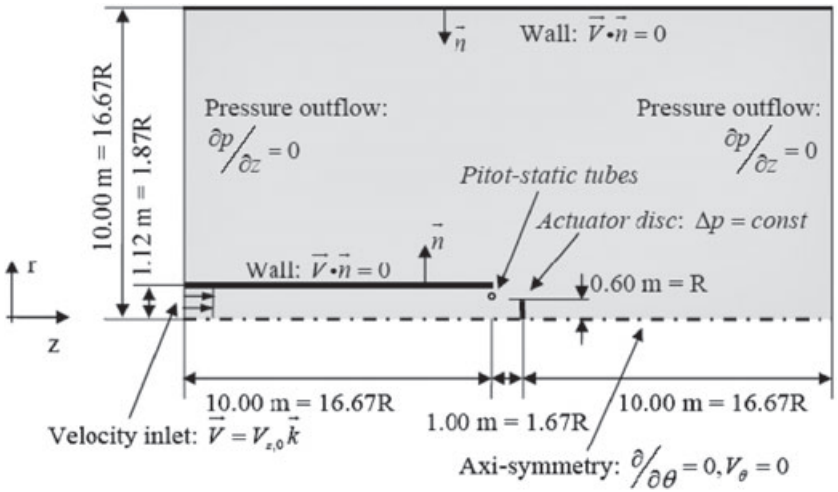

Figure 6. The conceptual model of an actuator disc placed in an open jet wind tunnel. The setup represents the model rotor in the open jet wind tunnel at the TUDelft. Flow direction is from left to right

contribution to $U_{\langle V\rangle}$ from the random uncertainty associated with determining the PLA over 54 recordings per (r, θ, z, θ_b)-point, estimated at 0.036, is minor compared with the typical $U_{\langle V\rangle}$ range. Hence, the sample size of 54 recordings is adequate.

Wall Effects

The wind tunnel setup does not perfectly replicate the conditions of a model rotor subject to unbounded flow, uniform at a distance far upstream. Two possible corrections are identified:

- Blockage correction: the ratio of the model rotor area to the wind tunnel jet area is finite.
- Non-uniformity correction: the Pitot-static tubes that record the dynamic pressure for W_{jet} are close to the rotor plane.

Both corrections are studied by numerically solving the discretized Euler equations with the commercial code Fluent. The domain is a simplified representation of the wind tunnel setup (see Figure 6). A uniformly loaded actuator disc model is used instead of a two-bladed rotor. The incompressible definition of the finite volume, cell-centred flow solver is used; the mass conservation and momentum equations are solved sequentially. The SIMPLEC algorithm, combined with the Rhie–Chow procedure to prevent checkerboarding of the pressure, is used for pressure–velocity coupling.

Grid and domain dependency studies are performed; both show monotonic convergence with reduced cell size and increased domain dimensions, respectively. Based hereupon, the dimensions of the domain are selected as shown in Figure 6, and the grid yields a discretization of the semi-actuator disc with 21 cell nodes. The jet area between the tunnel exit and the actuator disc is discretized with square cells of equal sizes. In the remainder of the domain, maximum cell stretching in both the z- and r-direction is set to 1.05.

To correct for wind tunnel blockage, the approach suggested by Glauert[22] is pursued; an equivalent unbounded air speed W_0^* is determined which yields the same velocity through the actuator disc, and hence the same thrust, as the inflow velocity $V_{z,0} = W_0$ set in the wind tunnel. With the superscript * indicating the equivalent unbounded condition, the equivalent velocity concept can be written as

$$c_T W_0^2 = c_T^*(W_0^*)^2 \tag{10}$$

$$W = W^* \tag{11}$$

DOI: 10.1002/we

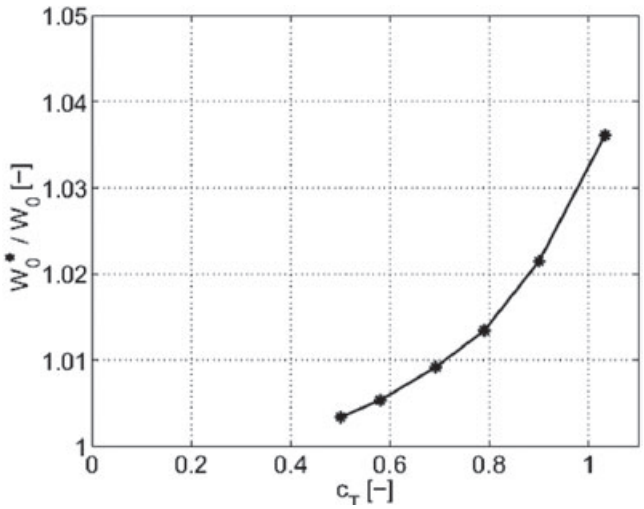

Figure 7. Ratio of equivalent unbounded air speed W_0^* *over inflow velocity* W_0 *versus thrust coefficient* c_T *from inviscid acuator disc computation*

In the unbound condition, the thrust can be written as

$$T^* = \frac{1}{2}\rho S c_T^* (W_0^*)^2 = 2W^*\rho S(W_0^* - W) \tag{12}$$

using one-dimensional momentum theory. Combining equations (10)–(12), Sørensen *et al.* derived[23]

$$\frac{W_0^*}{W_0} = \frac{W}{W_0} + \frac{1}{4}\frac{c_T}{W/W_0} \tag{13}$$

Now, W_0^*/W_0 can be determined (see Figure 7) by substituting the computational results in the right-hand side of equation (13). For W, the area weighted average of the computed axial velocity over the actuator disc is used. The current setting with $\lambda = 8$, $\theta_{c_{tip}} = 2^\circ$ yields $c_T = 0.80$ and hence $W_0^*/W_0 = 1.014$.

The computed inviscid velocity in the wind tunnel exit plane, where the Pitot-static tubes are located, is non-uniform; the flow speed is reduced towards the jet centre because of the proximity of the wind turbine model to the wind tunnel exit plane. For the current setting however, the local axial velocity W_{jet} at the radial position of the Pitot-static tubes is approximately equal to W_0; $W_{jet}/W_0 = 1.001$ is found. The main correction thus originates from wind tunnel blockage,

$$W_0^*/W_{jet} = W_0^*/W_0 \cdot \frac{1}{W_{jet}/W_0} = 1.013 \tag{14}$$

The corrected flow conditions now become $W_0^* = 5.57$ m s^{-1} and $\lambda^* = 7.90$, with $c_T^* = 0.77$.

Results

Azimuthal-averaged Axial Induction

A global analysis of the measured data is performed by a study of the azimuthal-averaged axial induction factor in the rotor plane.

No measurements are performed in the rotor plane itself. The velocity data from the three downstream planes, at $z/R_t = 0.0583$, 0.100 and 0.150, are used to construct the induction factor a in the rotor plane, with

$$a^* = 1 - \bar{W}/W_0^* \tag{15}$$

DOI: 10.1002/we

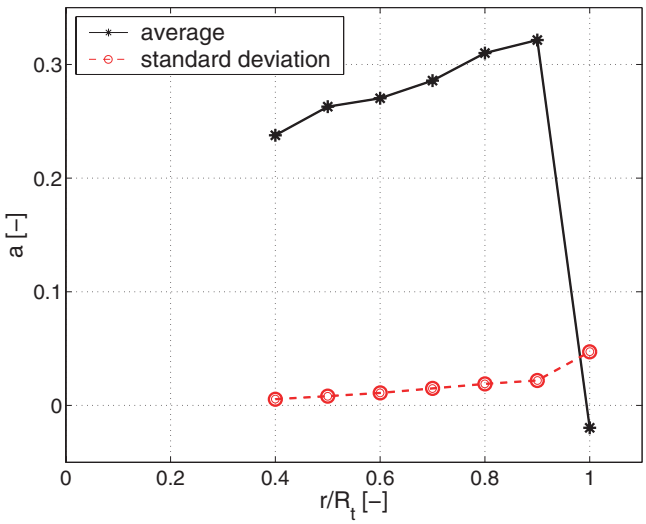

Figure 8. Axial induction factor a* *in the rotor plane, derived from a Least Squares fit of measurements at planes* z/R_t *= 0.0583, 0.100 and 0.150 downstream of the rotor plane*

In the three measurement planes, the hot-films are positioned at identical (r, θ)-points. With the blade at a given angle θ_b, the azimuthal-averaged axial velocity $\bar{W}$ at each r-coordinate is determined for all three measurement planes. The assumed linear function $\bar{W} = \bar{W}(z)$ is fitted to the measured data in the Least Squares sense for equal radii and is used to extrapolate $\bar{W}$ to the rotor plane. Using equation (15), a^* is determined in the rotor plane for each recorded blade azimuth angle θ_b. The average and standard deviation of a^* over the range $\theta_b = 0^\circ, 2^\circ, \ldots, 358^\circ$ is shown in Figure 8.

A radial dependency in a^* can be observed. The increased standard deviation of a^* near the blade tip can be explained by small asymmetries in the strong tip vortex.

One-dimensional momentum theory is used to determine the local thrust coefficient at a given radius, $C_t^*(r)$, in the rotor plane

$$C_t^* = 4a^*(1-a^*). \tag{16}$$

For each recorded blade azimuth angle θ_b, the rotor thrust coefficient C_T^* is computed by integrating $C_t^*(r)$ across the rotor disc under the assumptions that $C_t^*(R_t) = 0$ and $C_t^*(0) = C_t^*(r_1)$, with r_1 the radius of the most inboard data point. The average over the θ_b range is found to be $C_T^* = 0.72$. Force measurements on the rotor, using strain gauges, yield $C_T^* = 0.77 \pm 0.078$. The difference in C_T from momentum theory and force measurements is within the uncertainty bounds for both approaches. An exact match is not expected, however, as the infinite blades assumption of one-dimensional momentum theory is violated by the two-bladed rotor.

Trends in Azimuth Angle-dependent Velocity

Not only the phased-lock *average* 'true' velocity $\langle\vec{V}\rangle$, but also the phase-locked *standard deviation* of the effective velocity $s_{V_{eff}}$, determined over 54 blade rotations, yields information on the wake flow. $s_{V_{eff}}$ appears to be an effective measure of the wake passage. Fluctuations due to wake turbulence result in a local $s_{V_{eff}}$ increase when a wake passes a given data point (r, θ, z). The wake evolution in the near-wake region can be seen in Figure 9.

The deformation and diffusion of the wake, while convected downstream, can be observed. Non-uniform induction yields deformation of the wake from its original linear shape when trailed from the blade trailing edge. The concentrated tip vortices induce a strong flow field locally near the tip vortex, with corresponding large induced velocity gradients. Hence, wake deformation increases towards the tip vortices.

DOI: 10.1002/we

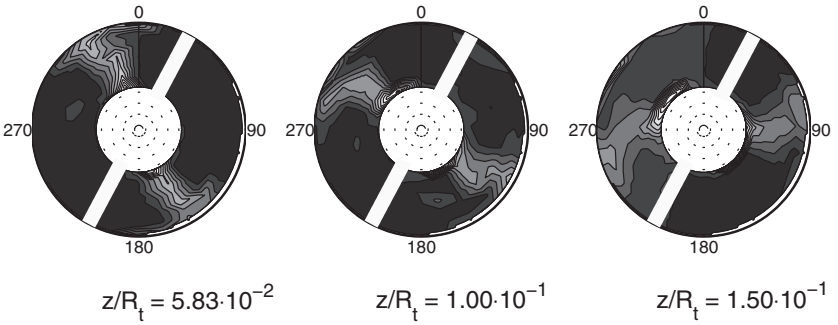

Figure 9. Standard deviation of hot-film effective velocity s_{veff} at three downstream planes for a blade orientation of $\theta_b = 28^\circ$. The blades rotate clockwise; the freestream wind is directed away from the observer

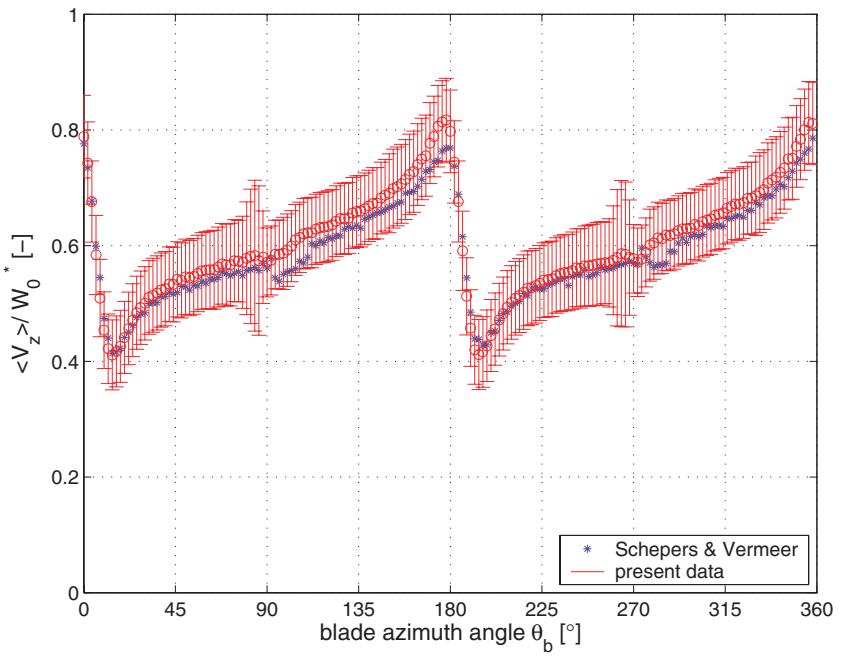

Figure 10. $\langle V_z \rangle / W_0^*$ versus θ_b at (r/R_t, θ, z/R_t) = (0.7, 180°, 0.100) for Schepers[15] and present data. Uncertainty bounds are included for present data. Blade passage: $\theta_b = 0^\circ$, 180°; wake passage: $\theta_b \approx 90^\circ$, 270°

The analysis of PLA results commences with a comparison of $\langle \vec{V} \rangle$ derived with the new and traditional single-sensor hot-film data reduction technique. Furthermore, current results are compared with results published by Schepers[15], measured on the same rotor, in the same wind tunnel, under the same conditions, $\Psi = 0^\circ$, $\theta_{c_{tip}} = 2^\circ$, $W_0^* = 5.57$ m s^{-1} and $\lambda^* = 7.90$, that are obtained from 10 instead of 54 recordings per (r, θ, z, θ_b)-point. The presently measured data set is processed using both the new and the traditional single-sensor hot-film data reduction technique. Comparisons are made for all three velocity components, $\langle V_r \rangle$, $\langle V_\theta \rangle$ and $\langle V_z \rangle$.

As both data reduction techniques derive $\langle V_z \rangle$ identically, the present $\langle V_z \rangle$ data are plotted in Figure 10 using the new method only. The agreement between present and previously published $\langle V_z \rangle$ data is within the uncertainty bounds of the present measurements. For the hot-film position plotted in Figure 10, maximum and average absolute $\langle V_z \rangle$ differences are 0.3 and 0.1 m s^{-1}. The repeatability in $\langle V_z \rangle$ between the two measurement campaigns gives confidence in the present data set.

DOI: 10.1002/we

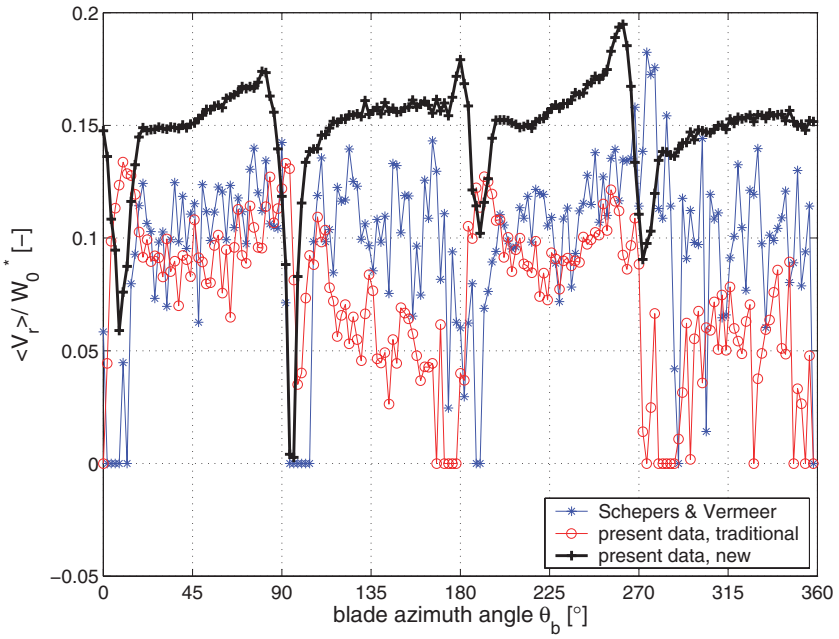

Figure 11. $\langle V_r \rangle / W_0^*$ *versus* θ_b *at* $(r/R_t, \theta, z/R_t) = (0.7, 180^\circ, 0.100)$ *for Schepers and Vermeer*[15] *and present data. Blade passage:* $\theta_b = 0^\circ, 180^\circ$*; wake passage:* $\theta_b \approx 90^\circ, 270^\circ$

Comparing the results for $\langle V_r \rangle$ and $\langle V_\theta \rangle$ (see Figures 11 and 12 for a typical example) yields that the order of magnitude of a velocity component is equal for all three velocity sets. The characteristics of the velocity distribution as a function of θ_b differ significantly, however, between the two data reduction techniques. The wiggles in both $\langle V_r \rangle$ and $\langle V_\theta \rangle$, present with the traditional approach, are reduced for the new technique, thereby better identifying blade and wake passages. The proposed technique yields the direction of the velocity component as part of its solution (see Figure 12). Whereas the traditional approach predicts $\langle V_\theta \rangle$ to be positive everywhere, the new data reduction predicts sign changes. Qualitative comparison with near-wake velocity studies by Ebert and Wood[6] and Vermeer[14] confirms the $\langle V_\theta \rangle$ shape.

The new data reduction technique yields more detail in the $\langle V_r \rangle$ and $\langle V_\theta \rangle$-distribution than the traditional technique. The remainder of the discussion is hence based upon the velocity derived using the new approach.

To help explain the observed trends in near-wake velocities, a typical lifting line wake vortex model is presented in Figure 13. A line of bound circulation, the lifting line, spans the blade. Circulation is trailed into the wake to form a vortex sheet.

The axial flow condition ideally results in θ-independent PLA velocity $\langle \vec{V} \rangle$, when $\langle \vec{V} \rangle$ is corrected for θ_b-phase shifts that occur with variations in the θ-coordinate. Averaging over the θ-positions yields $\overline{\langle \vec{V} \rangle}$. For the combination of three radial with three downstream locations, $\overline{\langle V_r \rangle}$, $\overline{\langle V_\theta \rangle}$, and $\overline{\langle V_z \rangle}$ are plotted in Figures 14–16.

The blade passages are located at $\theta_b = 90^\circ$ and 270°. At the blade passages, a local $\langle V_z \rangle$-maximum followed by a local $\langle V_z \rangle$-minimum and a local $\langle V_\theta \rangle$-minimum are found. The minima and maxima in $\langle V_z \rangle$ and $\langle V_\theta \rangle$ at the blade passages are induced by the bound vortex; the trends at the blade passages agree with the orientation of the bound circulation vector, pointing outboard as can be seen in Figure 13 using the right-hand rule. The amplitude of the peaks is reduced when going downstream for a given radial position, since the distance to the bound circulation is increased.

Three causes are identified to explain $\langle V_r \rangle$ during a blade passage. First, from the simple vortex wake model (see Figure 13), the bound circulation is expected to induce a local $\langle V_r \rangle$-minimum followed by a local $\langle V_r \rangle$-maximum, resulting in an overall $\langle V_r \rangle$-increase with a blade passage. Second, when considering a lifting *surface*

DOI: 10.1002/we

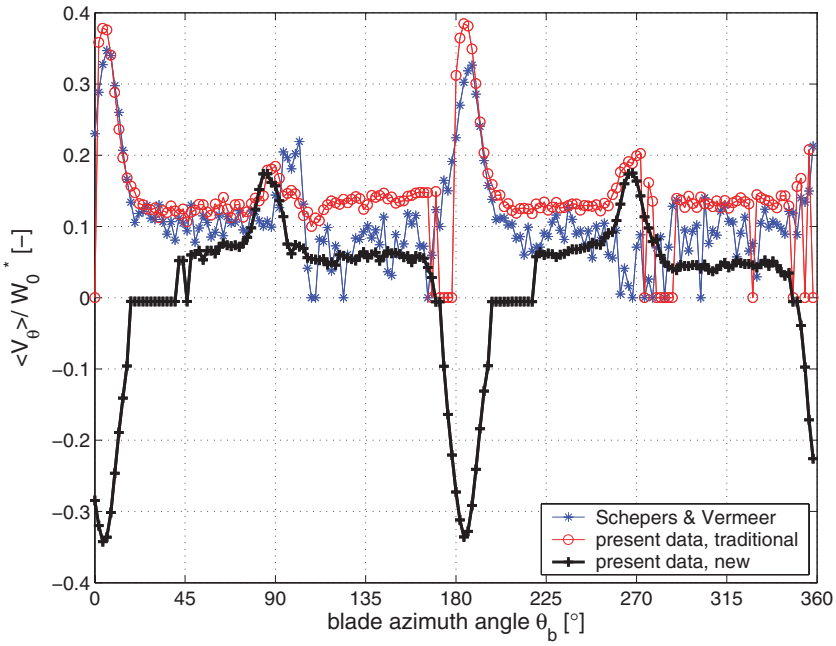

Figure 12. $\langle V_\theta \rangle / W_0^*$ *versus* θ_b *at* (r/R_t, θ, z/R_t) = *(0.7, 180°, 0.100) for Schepers*[15] *and present data. Blade passage:* θ_b = *0°, 180°; wake passage:* $\theta_b \approx$ *90°, 270°*

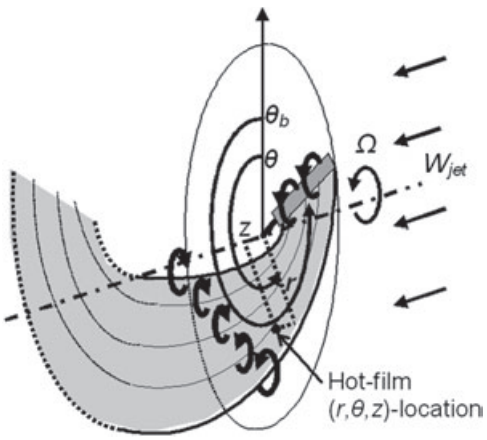

Figure 13. Typical vortex wake model. The direction of bound and trailed circulation is indicated as is a hot-film position in cylindrical coordinates

instead of the lifting *line* vortex wake model, varying bound circulation across the blade span introduces bound circulation oriented in the chordwise direction that trails into the wake. During a blade passage, chordwise-bound circulation induces a $\langle V_r \rangle$-contribution; negative for a bound circulation increase when going outboard and vice versa. Third, the pressure difference between the blade pressure and the suction side induces radially inboard $\langle V_r \rangle$ near the tip and radially outboard $\langle V_r \rangle$ near the root. Observations from Figures 14 to 16 agree with the three mentioned $\langle V_r \rangle$-trends. Note that in general $\langle V_r \rangle$ is positive, corresponding to an expanding flow.

With regard to the wake passage, the inviscid vortex wake model shown in Figure 13 only explains the $\langle V_r \rangle$-behaviour. Passage of the vortex sheet results in a step change in $\langle V_r \rangle$. The orientation of the trailed circulation determines the sign of the step change. The signs of the step changes, negative for $r/R_t = 0.4$ and

DOI: 10.1002/we

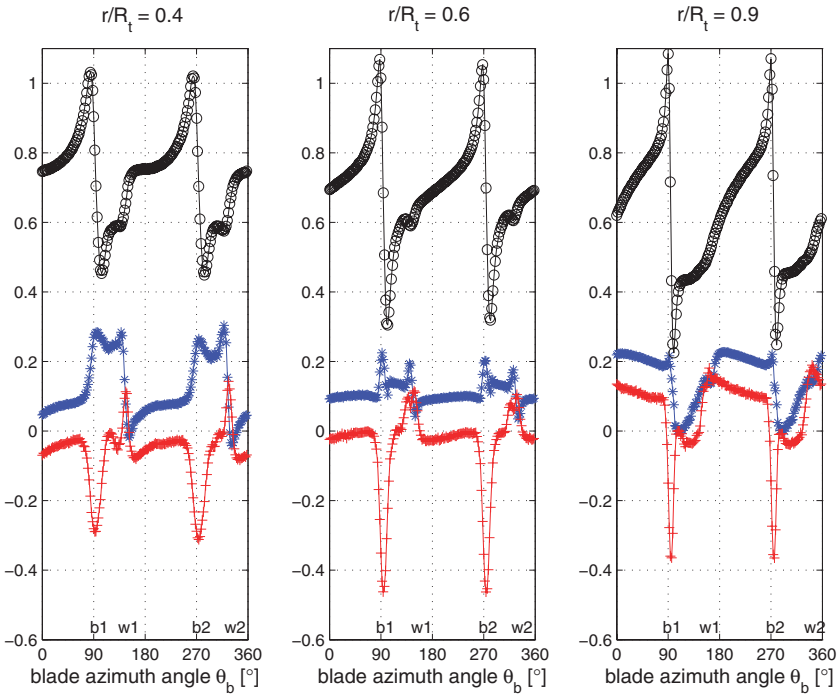

Figure 14. Non-dimensional velocity versus θ_b *at* $(\theta, z/R_t) = (90^\circ, 0.0583)$ *for radial locations* $r/R_t = 0.4, 0.6$ *and 0.9.* $\langle \overline{V_r} \rangle / W_0^*$: *, $\langle \overline{V_\theta} \rangle / W_0^*$: +, $\langle \overline{V_z} \rangle / W_0^*$: ○. *The passages of the first and second blade and their corresponding wakes are indicated by (b1, w1) and (b2, w2) respectively*

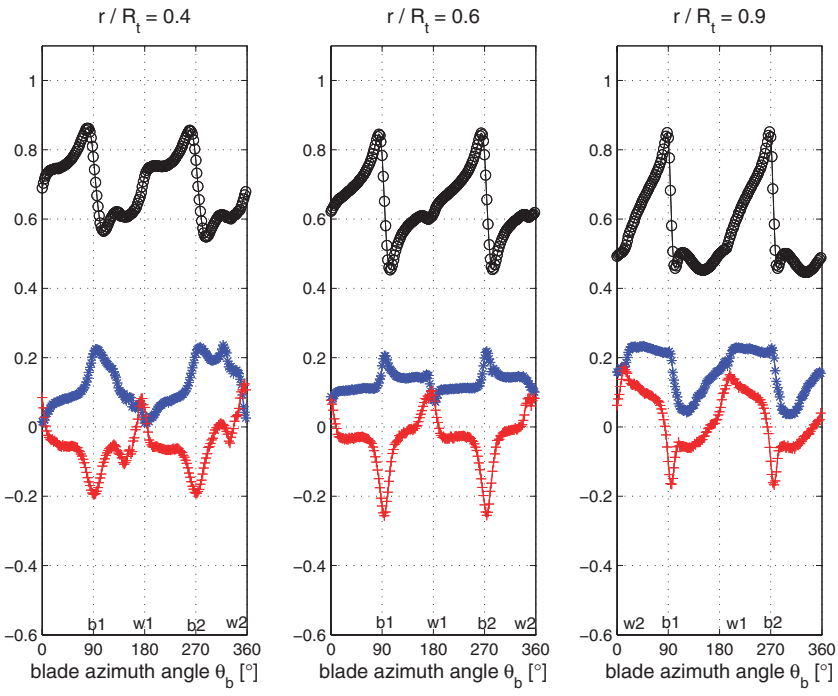

Figure 15. Non-dimensional velocity versus θ_b *at* $(\theta, z/R_t) = (90^\circ, 0.100)$ *for radial locations* $r/R_t = 0.4, 0.6, 0.9$. $\langle \overline{V_r} \rangle / W_0^*$: *, $\langle \overline{V_\theta} \rangle / W_0^*$: +, $\langle \overline{V_z} \rangle / W_0^*$: ○. *The passages of the first and second blade and their corresponding wakes are indicated by (b1, w1) and (b2, w2), respectively*

DOI: 10.1002/we

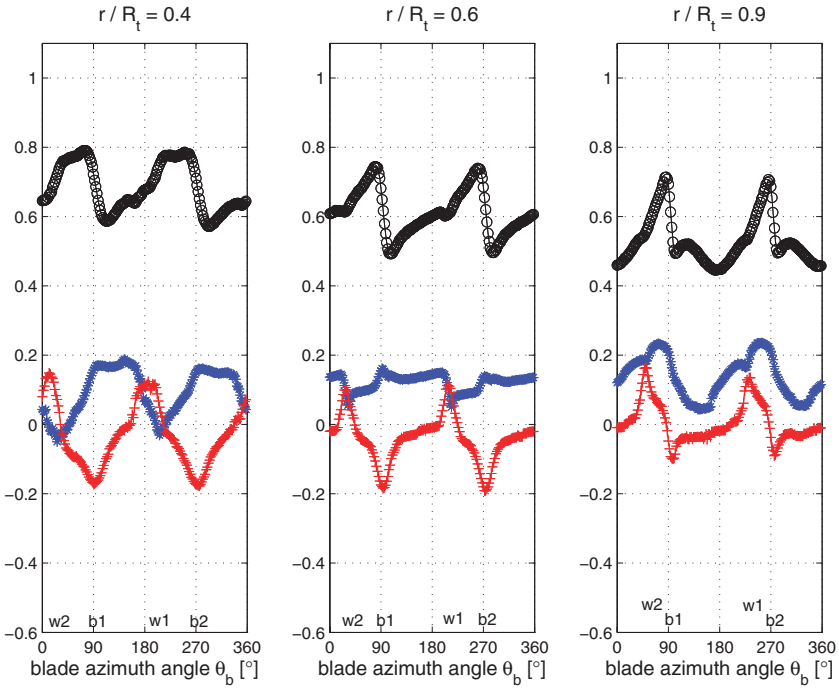

Figure 16. Non-dimensional velocity versus θ_b *at* (θ, z/R_t) = (90°, 0.150) *for radial locations* r/R_t = 0.4, 0.6, 0.9. $\overline{\langle V_r \rangle}/W_0^*$: *, $\overline{\langle V_\theta \rangle}/W_0^*$: +, $\overline{\langle V_z \rangle}/W_0^*$: ○. *The passages of the first and second blade and their corresponding wakes are indicated by (b1, w1) and (b2, w2), respectively*

0.6 and positive for $r/R_t = 0.9$, agree with a typical variation of bound circulation on a rotating blade and the corresponding orientation of the trailed circulation in the wake.

Viscous effects are responsible for the trends in $\langle V_\theta \rangle$ and $\langle V_z \rangle$ with wake passages. The local $\langle V_z \rangle$ minimum and $\langle V_\theta \rangle$-maximum represent the momentum loss due to viscous drag associated with the boundary layer that trails from the blade surface into the wake. For the current high-λ condition, the viscous drag mainly acts in the tangential direction; its effect in the axial direction is small.

The local $\langle V_z \rangle$-minimum at the wake passage represents an axial momentum loss, hence the contribution to the thrust due to viscous drag. The local $\langle V_\theta \rangle$-maximum at the wake passage is larger than zero and hence in the same direction as the rotor rotation, indicating that the wake is dragged along in the rotor rotation direction. The local $\langle V_\theta \rangle$-maximum corresponds to a reduction in the angular momentum of the flow and hence a reduction in the blade torque.

Local Angle of Attack

Blade Element Momentum and vortex wake methods utilize airfoil models to determine the blade forces for a given velocity distribution in the rotor plane. The airfoil models require a two-dimensional angle of attack α.

For a two-dimensional airfoil, α is defined by the angle between the undisturbed flow and the airfoil chord. On a rotating blade, however, the flow passing a blade section is bent because of the blade rotation; bound circulation induces local velocities; and three-dimensional effects are introduced by tip and root vortices. Hence, α is difficult to define.

Methods to estimate α include an azimuthal-averaged axial velocity method by Hansen *et al.*,[24] a combined load-velocity method by Shen *et al.*[25] and a blade pressure method by, e.g. Van Rooij *et al.*[26] Furthermore, α-definition issues are avoided by using a measured local inflow angle instead, e.g. in a discussion by Schreck and Robinson on results of the National Renewable Energy Laboratory (NREL) Unsteady Aerodynamics Experiment.[27]

DOI: 10.1002/we

The current experiment does not yield local blade loads; hence, only the azimuthal-averaged axial velocity method can be applied. The procedure to arrive at the azimuthal-averaged V_z in the rotor plane is similar to the determination of the azimuthal-averaged induction factor in the rotor plane.

Furthermore, α is determined from the present measurements with a modified version of the blade passage method by Sant [28]. The method is based on the observation that, with the blade represented by a lifting line, the contribution from the bound vortex to the $\langle V_z \rangle$-signal at given (r, θ, z)-location is antisymmetric around the point of blade passage, $\theta_{b_{blade}} = \theta$. The average of the local $\langle V_z \rangle$-minimum and maximum at a blade passage is not influenced by the local bound circulation. When determined at the rotor plane, the blade passage average axial velocity can be used to determine α.

A linear relation between the blade passage $\langle V_z \rangle$-average and z is fitted in the Least Squares sense to the recordings at the three downstream measurement planes for given r and θ. Extrapolation of the linear function yields the value for the blade passage $\langle V_z \rangle$-average in the rotor plane that is used subsequently to determine α. The average and standard deviatioin of α are subsequently determined for the sample of 24 θ-points per given r.

The difference in mean $\alpha(r)$ between the two methods is smaller than the corresponding standard deviations (see Figure 17). For the model rotor, with its relatively high solidity, the difference between the azimuthal-averaged axial induction and the local axial induction, both in the rotor plane, is therefore insignificant. For a rotor having lower solidity, differences in the prediction of α between the two methods are expected.

α_{max}, found at the most inboard measurement position, is 8.5°. Measurements on the NACA0012 airfoil at $Re = 0.15 \times 10^6$ yield a static stall angle $\alpha_{stall} = 10.6°$, suggesting that stall is not present on the blades. Detailed blade loads that could confirm this suggestion are not measured however.

Wake Convection

The viscous wake is associated with a distinct increase in the standard deviation of the effective velocity s_{Veff}. For a given hot-film location (r, θ, z), the wake passage angle $\theta_{b,wake}$ is detected using the s_{Veff}-increase. The wake age $\Delta\theta$ is determined from

$$\Delta\theta_{b,wake} = \theta_{b,wake} - \theta_{b,blade} \tag{17}$$

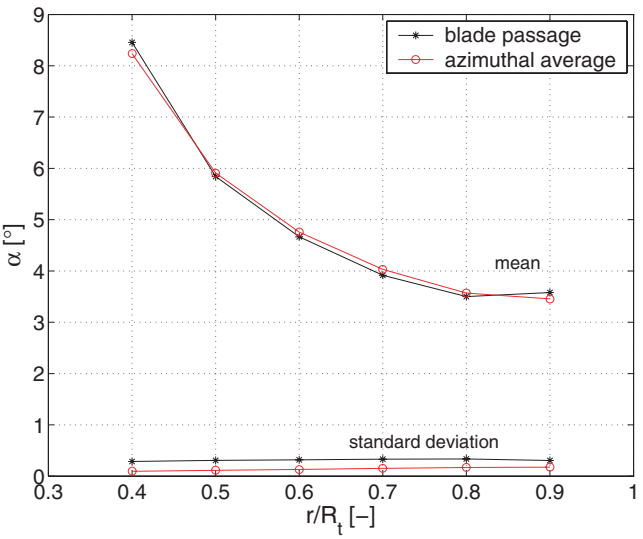

Figure 17. Angle of attack α *versus* r/R_t. α *is determined with both the azimuthal average and the blade passage method*

DOI: 10.1002/we

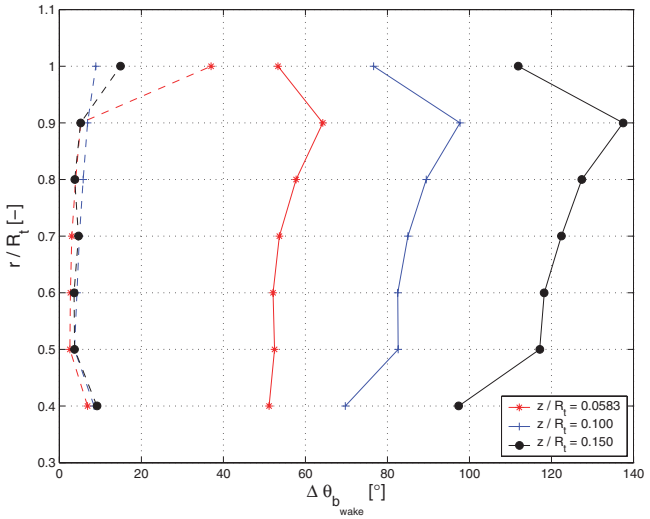

Figure 18. Average (solid line) and standard deviation (dashed line) of the wake age. At each hot-film (r/R_t, z/R_t)*-coordinate, wake age recordings are taken for every* θ*-coordinate,* $\theta = 0^\circ, 15^\circ, \ldots, 345^\circ$*, and the average and standard deviation are determined*

with $\theta_{b,blade}$ the blade passage angle. For a given hot-film location (r, θ, z), $\theta_{b,blade}$ equals θ or ($\theta + 180^\circ$), when considering the passage of the first and the second blade, respectively. The viscous wake velocity is found by averaging the measured $\langle V_z \rangle$, $\langle V_\theta \rangle$ and $\langle V_r \rangle$ over the viscous wake passage.

Wake age in the mid-span region increases when going outboard (see Figure 18). Correspondingly, the wake axial velocity decreases when going outboard (see Figure 19). Both observations agree with the higher axial induction factor seen when going outboard in Figure 8. Both the viscous wake radial and tangential velocity are positive in the mid-span region. The viscous wake thus moves outboard and rotates in the same direction as the blades, indicating it is dragged along in the rotor rotation direction.

The reduced viscous wake age and increased wake axial velocity for $r/R_t = 1.0$, compared with $r/R_t = 0.9$, shown in Figures 18 and 19, indicate a roll-up of the viscous wake into the tip vortex, since the tip vortex is convected downstream faster than the wake in the mid-span region. Without roll-up of the viscous wake into the tip vortex, the wake axial velocity would be reduced instead of increased when approaching $r/R_t = 1.0$, because of the dominant contribution of the tip vortex to the axial induction velocity near $r/R_t = 1.0$. The largest standard deviations in both the wake age and wake velocity are found for $r/R_t = 1.0$, because of the dominant influence the tip vortex has on the local flowfield, combined with the tip vortex geometry that is not perfectly axisymmetric.

Conclusions

A wind tunnel measurement campaign focused on a wind turbine model rotor in both axial and yawed flow conditions is conducted. Measurements of the tip vortex geometry and the velocity in the near-wake of a two-bladed model rotor are performed in an open jet wind tunnel. Additionally, axial force measurements on the rotor are taken. The near-wake velocity measurements of the baseline case, the rotor in axial flow, are discussed here. Three downstream planes are traversed by a single-sensor hot-film probe.

A new data reduction method based on the asymmetrical response of the hot-film probe to the flow vector enables the derivation of the PLA three-dimensional flow velocity vector. The traditional data reduction method

DOI: 10.1002/we

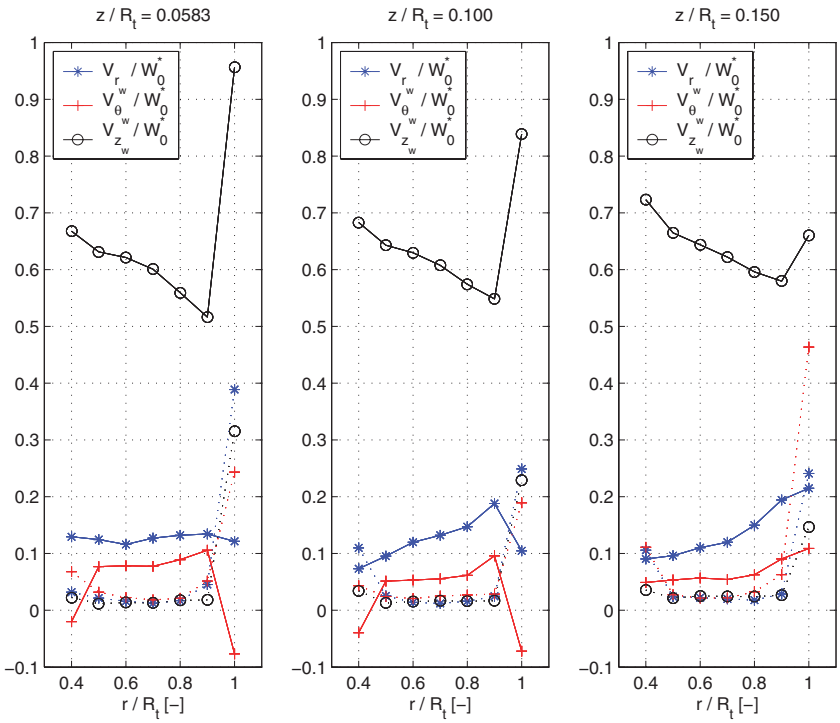

Figure 19. Average (solid line) and standard deviation (dashed line) of the mean viscous wake velocity during a wake passage. Left plot: $z/R_t = 0.0583$*, centre plot:* $z/R_t = 0.100$*, right plot:* $z/R_t = 0.150$*. The mean viscous wake velocity is determined at every hot-film location and the average and standard deviation are taken over all* θ*-coordinates,* $\theta = 0^\circ, 15^\circ, \ldots 345^\circ$*, for a given* $(r/R_t, z/R_t)$*-position*

for single-sensor hot-films only yields the magnitudes of the components of the PLA flow velocity vector, not its directions.

The traditional and the new data reduction technique are applied to the same data set. When comparing the PLA radial and tangential velocity distributions, the results from the new approach are less noisy and the direction of the velocity components is part of the result. Hence, the new data reduction method is preferred to the traditional method.

The data quality is further assessed by estimating the random measurement uncertainty, by studying wind tunnel wall effects and by checking repeatability with published measurements. These assessments are needed to properly compare experimental data with models.

The experimental determination of the unsteady velocity field assists in a better understanding the near-wake aerodynamics behind the model HAWT. Both the phase-locked average and standard deviation of the velocity yield information; the standard deviation is an effective measure of the wake passage.

The observed trends in the PLA velocity in the near-wake can be explained by considering a typical inviscid vortex wake model combined with viscous wake effects. The wake deformation and roll-up into the tip vortex can be observed from the derived age and convection velocity of the viscous wake. The flow velocity measurements are also used to determine the azimuthal-averaged axial induction in the rotor plane and angle of attack on the blades. The azimuthal average and the local blade passage approach arrive at an equivalent angle of attack distribution across the blade span.

In conclusion, the analysis of the detailed unsteady flow velocity measurements enables an understanding of the near-wake aerodynamics of the model wind turbine rotor subject to the baseline axial flow condition. In a next paper, the influence of yaw misalignment on the near-wake aerodynamics is discussed.

DOI: 10.1002/we

References

1. Leishman JG. Challenges in modelling the unsteady aerodynamics of wind turbines. *Wind Energy* 2002; 5: 85–132.
2. Snel H. Review of the present status of rotor aerodynamics. *Wind Energy* 1998; 1:46–69.
3. Snel H. Review of aerodynamics for wind turbines. *Wind Energy* 2003; 3: 203–211.
4. Simms D, Schreck S, Hand M, Fingersh LJ. Nrel unsteady aerodynamics experiment in the NASA-Ames wind tunnel: a comparison of predictions to measurements. Technical Report NREL/TP-500-29494, NREL, Boulder, CO.
5. Vermeer LJ, Sørensen JN, Crespo A. Wind turbine wake aerodynamics. *Progress in Aerospace Sciences* 2003; 39: 467–510.
6. Ebert PR, Wood DH. The near wake of a model horizontal-axis wind turbine—I. Experimental arrangements and initial results. *Renewable Energy* 1997; 12: 225–243.
7. Ebert PR, Wood DH. The near wake of a model horizontal-axis wind turbine—II. General features of the three-dimensional flowfield. *Renewable Energy* 1999; 18: 513–534.
8. Ebert PR, Wood DH. The near wake of a model horizontal-axis wind turbine, part 3: properties of the tip and hub vortices. *Renewable Energy* 2001; 22: 461–472.
9. Grant I, Parkin P, Wang X. Optical vortex tracking studies of a horizontal axis wind turbine in yaw using laser-sheet, flow visualisation. *Experiments in Fluids* 1997; 23: 513–519.
10. Grant I, Mo M, Pan X, Parkin P, Powell J, Reinecke H, Shuang K, Coton F, Lee D. An experimental and numerical study of the vortex filaments in the wake of an operational, horizontal axis, wind turbine. *Journal of Wind Engineering and Industrial Aerodynamics* 2000; 85:177–189.
11. Grant I, Parkin P. A DPIV study of the trailing vortex elements from the blades of a horizontal axis wind turbine in yaw. *Experiments in Fluids* 2000; 28:368–376.
12. Parkin P, Holm R, Medici D. The application of PIV to the wake of a wind turbine in yaw. *Proceedings of the 4th International Symposium on Particle Image Velocimetry*, Gottingen, Germany, 2001.
13. Medici D, Alfredsson PH. Measurements on a wind turbine wake: 3D effects and bluff body vortex shedding. *Wind Energy* 2006; 9: 219–236.
14. Vermeer LJ. A review of wind turbine wake research at TUDelft, AIAA-2001-0030. *20th ASME Wind Energy Symposium, 39th Aerospace Sciences Meeting and Exhibit*, Reno, NV, January 2001; 1–11.
15. Schepers JG. An engineering model for yawed conditions, developed on basis of wind tunnel measurements. *AIAA*-1999-0039 18th ASME Wind Energy Symposium, 37th Aerospace Sciences Meeting and Exhibit, Reno, NV, January 1999; 164–174.
16. Haans W, Sant T, van Kuik GAM, van Bussel GJW. Measurement of tip vortex paths in the wake of a HAWT under yawed flow conditions. *Journal of Solar Energy Engineering* 2005; 127: 456–463.
17. Haans W, Sant T, van Kuik GAM, van Bussel GJW. Stall in yawed flow conditions: a correlation of blade element momentum predictions with experiments, *Journal of Solar Energy Engineering* 2006; 128:472–480.
18. Haans W, Sant T, van Kuik GAM, van Bussel GJW. Velocity measurements in the near wake of a horizontal axis wind turbine. *31st European Rotorcraft Forum*, Florence, Italy, September 2005; 61.1–61.14.
19. Bruun HH. *Hot-Wire Anemometry*. Oxford Science Publications, Oxford, UK, 1995.
20. AIAA. Assessment of experimental uncertainty with application to wind tunnel testing. Technical Report S-071A-1999, AIAA, Reston, VA, 1999.
21. AIAA. Assessing experimental uncertainty—supplement to AIAA S-071A-1999. Technical Report G-045-2003, AIAA, Reston, VA, 2003.
22. Glauert H. Airplane propellers. In *Aerodynamic Theory*, Durand WF (ed.), chapter Division L, Dover Publications, New York, 1963, 169–360.
23. Sørensen JN, Shen WZ, Mikkelsen R. Wall correction model for wind tunnels with open test section. In *The Science of Making Torque from Wind*, van Kuik GAM (ed.). European Wind Energy Association EWEA and the European Academy for Wind Energy EAWE: Delft, The Netherlands, April 2004; 196–202.
24. Hansen MOL, Sørensen NN, Sørensen JN, Michelsen JA. Extraction of lift, drag and angle of attack from computed 3-D viscous flow around a rotating blade. *EWEC 1997*, Dublin, Ireland, October 1997; 499–501.
25. Shen WZ, Hansen MOL, Sørensen JN. Determination of angle of attack (AOA) for rotating blades. *EUROMECH Colloquium 464b Wind Energy*, Peinke J, Schaumann P, Barth S (eds). Oldenburg, Germany, Springer-Verlag: Berlin, 2006; 205–209.
26. Van Rooij RPJOM, Timmer WA, Bruining A. Determination of the local inflow angle on rotating blades. *Proceedings of the World Wind Energy Conference and Exhibition*, Berlin, Germany, July 2002.
27. Schreck S, Robinson M. Rotational augmentation of horizontal axis wind turbine blade aerodynamic response. *Wind Energy* 2002; 5:133–150.

DOI: 10.1002/we